ACS OMEGA

http://pubs.acs.org/journal/acsodf

Article

Methane Gas Cofiring Effects on Combustion and NO_x Emission in 550 MW Tangentially Fired Pulverized-Coal Boiler

Kang-Min Kim, Gyu-Bo Kim, Byoung-Hwa Lee, Chung-Hwan Jeon,* and Joon-Ho Keum

Cite This: *ACS Omega* 2021, 6, 31132−31146

Read Online

ACCESS | Metrics & More | Article Recommendations

ABSTRACT: A shift from coal to liquefied natural gas for electricity generation can mitigate CO_2 emissions and respond to the intermittent and variable characteristics of renewable energy. With this objective, numerical simulation was performed in this study to determine the optimal position of the methane injector and evaluate the achievable reduction in NO_x emissions before applying methane cofiring to an existing 550 MW tangentially fired pulverized-coal boiler (Boryeong Unit 3). The combustion and NO_x reduction in the furnace were intensively analyzed based on the methane cofiring rate (up to 40%). The optimal position of the methane injector was found to be inside the oil port based on the spatial distribution of NO_x and the stoichiometric ratio along the furnace height. The NO_x reduction rate was logarithmically proportional to the methane cofiring rate, and compared to the base case, a 69.8% reduction was achieved at the 40% cofiring rate. In addition, the fraction of unburned char at the boiler outlet was equivalent to that of the existing boiler as the increase in the flow rates of the close-coupled and separated overfire air improved fuel and air mixing. Simultaneously, methane cofiring led to a reduction in the total fuel loss and CO emissions. Finally, this study showed that the recommended optimum cofiring rate was 20% based on the furnace exit gas temperature. Under the 20% methane cofiring condition, the boiler achieved a 57.3% reduction in NO_x emissions and a 7.4% improvement in fuel loss.

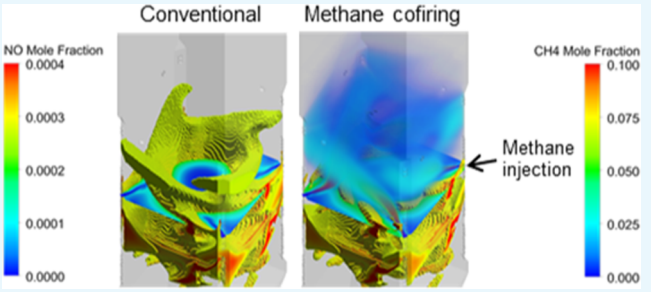

1. INTRODUCTION

The Paris Agreement on climate change (2015) prompted each participating country to set a goal to reduce greenhouse gas (GHG) emissions. Accordingly, the proportion of power generation using renewable energy and natural gas has gradually increased in an effort to reduce CO_2 emissions as well as harmful pollutants, including particulate matter. South Korea plans to triple the capacity of its renewable power-generation systems and substantially reduce the proportion of power generated from coal by shutting down 24 coal units by 2030.[1] Furthermore, to ensure a stable power supply, those coal units will be converted to liquefied natural gas (LNG) combined-cycle power plants. By replacing bituminous coal with natural gas, CO_2 emissions can be reduced by 43%, and SO_x, particulate matter, and mercury can be reduced by up to 100%. In contrast, NO_x emissions vary significantly depending on the combustion system; however, heavy-duty gas turbines (combined cycle) generate 60% lower NO_x emissions than supercritical coal boilers.[2]

Coal-fired power generation would certainly be discontinued in the long term; however, the use of all units cannot be discontinued immediately. Although construction plans for many new coal-fired power plants have been suspended in Korea, seven new units are to be built by 2030. In addition, the service lives of some units have been extended through retrofit projects to improve efficiency. Therefore, coal-fired power generation will continue to play an important role in the power grid during the transition period;[3] these facilities will supplement the intermittent power generation and the variability of renewable energy sources, such as wind and solar power, by improving the operating flexibility of the existing power plant systems, increasing efficiency, and reducing gas emissions including GHGs and NO_x.

Considering the aforementioned situation, the application of methane gas cofiring technology to an existing coal boiler was examined in this study. Cofiring coal with methane gas (or LNG) has the following benefits.[4] First, emissions can be reduced in proportion to the amount of coal replaced with methane gas. In particular, NO_x emissions can be potentially reduced beyond the gas cofiring rate by the reburning mechanism. Second, the method facilitates flexibility in fuel use. For example, if there is a problem with the availability of one fuel, it can be switched to another. This also helps in dealing with

Received: August 23, 2021
Accepted: September 29, 2021
Published: November 15, 2021

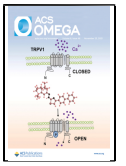

https://doi.org/10.1021/acsomega.1c04574
ACS Omega 2021, 6, 31132−31146

fuel price fluctuations. Third, methane gas cofiring improves operational flexibility. This accelerates the ramp-up and decreases the start-up time and can also significantly reduce the minimum load. Finally, compared to building a new LNG power plant, construction costs can be significantly reduced by utilizing the existing coal facilities and control systems.[5,6] Therefore, this study was conducted to evaluate the application of methane gas cofiring to a pulverized-coal boiler with the remaining lifespan and reduce NO_x emissions—a precursor of particulate matter—through the reburning mechanism.

Reburning technology was introduced in the 1990s by modifying pulverized-coal boiler facilities (Figure 1). Under

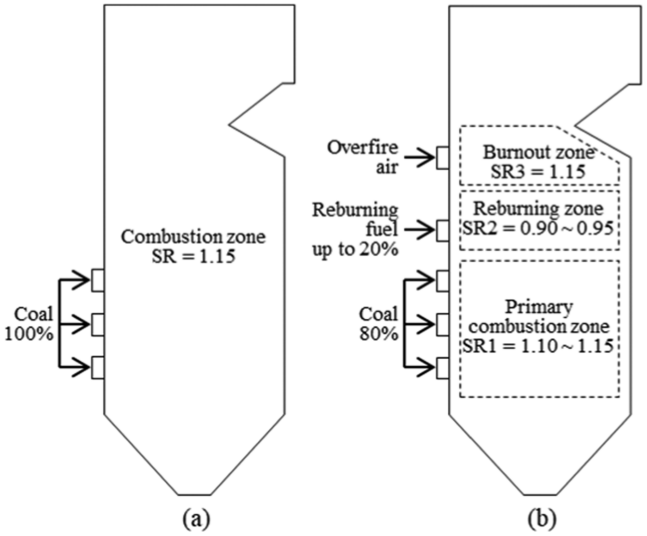

Figure 1. Schematic diagrams of (a) conventional coal firing and (b) gas reburning in a wall-fired boiler (SR: stoichiometric ratio).

this approach, up to 20% of the heat input is replaced with methane gas, which is a reburning fuel, and the fuel-rich gas is introduced above the primary combustion zone. Under oxygen-deficient conditions, methane is decomposed into hydrocarbon radicals, which react with NO in the flue gas to generate CN and NH_2 radicals. These radicals further react with NO to generate N_2. However, if the oxygen concentration is high in the reburning zone, CN and NH_2 react with oxygen to form NO.[7,8] Overfire air (OFA) is supplied to the burnout zone to completely burn the remaining fuels. In this process, even though additional NO_x is generated, it is in amounts lower than those reduced in the reburning zone. The application of methane gas reburning to coal-fired boilers can reduce NO_x by up to 60%.[9] As this requires the installation of methane gas injectors and OFAs, conventional gas reburning technology involves the modification of the furnace wall.

To reduce CO_2 and NO_x emissions, the application of cofiring to the large-scale utility boilers has been investigated using computational fluid dynamics (CFD). Adamczyk et al.[10] evaluated the usability of sewage sludge gasification gas as a reburning fuel in a 600 MW wall-fired utility boiler, focusing on NO_x reduction without modifying the boiler's design. Chernetskiy et al.[11] investigated the effects of introducing a reburning fuel port and OFA to a 387 MW utility boiler on NO_x and heat loss. Their study showed that the performance of coal as a reburning fuel can be increased by microgrinding and mechanical activation processes. Despite these previous CFD applications to evaluate the effect of reburning in utility boilers, limited data are available on the coal-methane cofiring in tangentially coal-fired boilers, which is the target of the current study. In 2021, Duke Energy completed the construction of its Marshall Steam Station in North Carolina, for natural gas cofiring. At this facility, the Marshall Unit 3, a 700 MW 8-corner tangentially fired boiler, is capable of up to 50% cofiring. To apply this technology, CFD was performed according to the reburning configurations, and NO_x was reduced by 20.8 and 56.6% with 10 and 50% natural gas cofiring, respectively.[12,13] Meanwhile, the current study sought to determine the optimal methane injector position, as well as the optimal methane cofiring rate, to achieve lower NO_x emissions and stable combustion without the water wall modification in the existing Boryeong Unit 3. To this end, the Marshall Unit 3 boiler served as a reference for the application of methane cofiring, while a simulation capable of accurately reflecting the true geometry and operating conditions of the boiler was established to better understand the effects of methane cofiring. This study also examined the mechanism for NO_x reduction based on the methane cofiring rate and provides relevant data for applying methane cofiring in tangentially fired pulverized-coal boilers.

2. BOILER DESCRIPTIONS

2.1. Boiler Specifications and Simulation Geometry.

Boryeong Power Plant Unit 3, the target system for applying methane cofiring in this study, is a 550 MW tangentially fired pulverized-coal boiler (Figure 2). At the end of 2019, the steam temperatures of the main steam heater and reheater of the boiler increased from 538/538 to 596/596 °C as part of an upgrade from supercritical to ultra-supercritical conditions through an efficiency improvement project. The thermal load of the furnace was unchanged because the water wall composed of spiral and

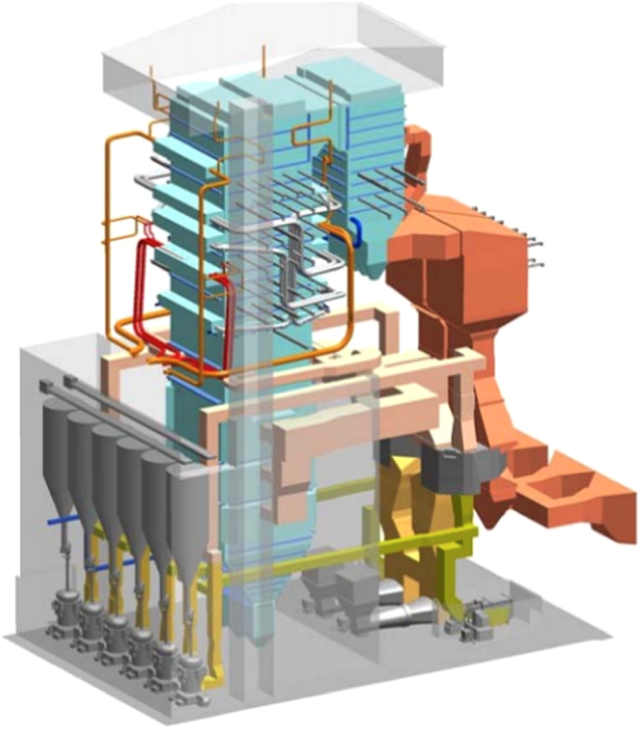

Figure 2. Three-dimensional (3D) representation of the Boryeong Power Plant Unit 3. The system excluding the rear pass is approximately 16.5 × 16.5 × 87 m.

https://doi.org/10.1021/acsomega.1c04574
ACS Omega 2021, 6, 31132−31146

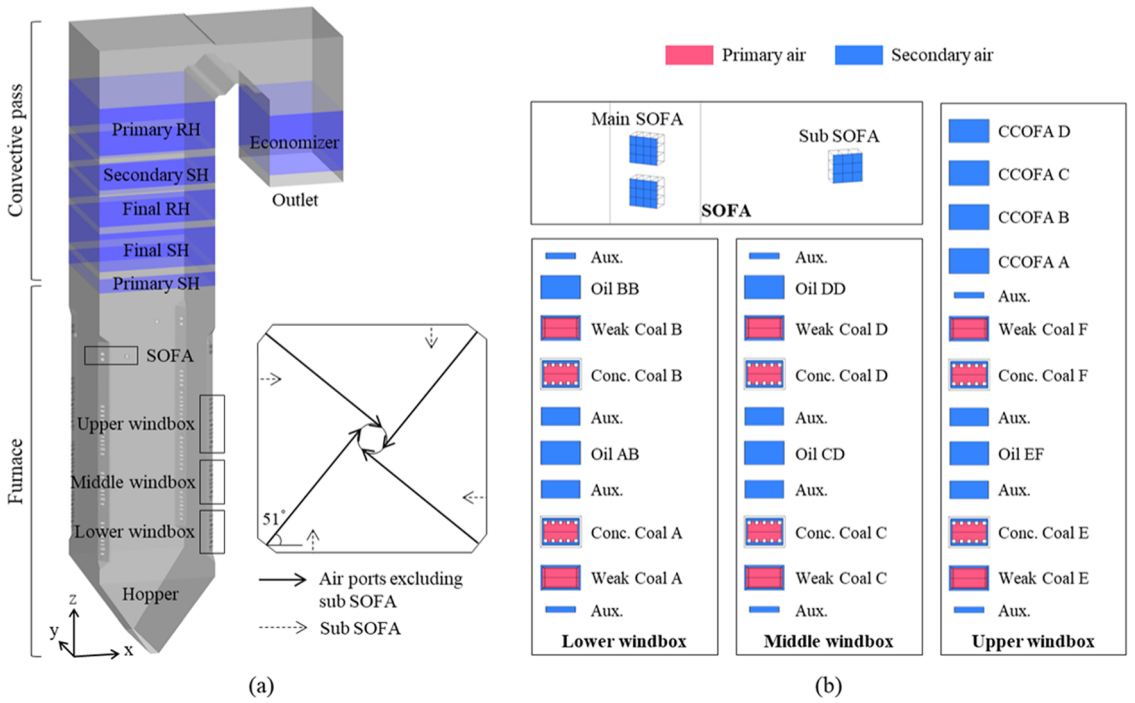

Figure 3. (a) Boiler geometry and burner direction and (b) burner arrangement used in CFD. Aux.: auxiliary, Conc.: concentrated, CCOFA: close-coupled overfire air, RH: reheater, SH: superheater, and SOFA: separated overfire air.

Table 1. Properties of Coal Used in the CFD Modeling

proximate analysis (wt %, as received)				ultimate analysis (wt %, dry ash-free basis)					
fixed carbon	volatiles	ash	moisture	C	H	O	N	S	calorific value (kcal/kg, as received)
41.19	32.77	9.87	16.17	83.60	5.86	8.53	1.54	0.48	5673

vertical tubes was not replaced, while heat transfer areas were added to the superheaters (SHs) and reheaters (RHs). In the furnace, the coal burner nozzle tip was replaced to improve flame stability and reduce unburned char and NO_x. In addition, a separated overfire air (SOFA) section was added to reduce NO_x through additional air staging at the top of the furnace. The SOFA section is composed of 12 ports, which include eight main ports and four subports. The main ports were installed at two levels, at the four corners of the furnace, similar to conventional close-coupled overfire air (CCOFA) systems, and the subports were installed on the water wall. In addition, several systems, including coal milling, were replaced.

Figure 3a presents the geometry of the boiler used in this study. The burners at each corner inject pulverized coal and air at an angle of 6° from the center to create a spiral flow, which rises along the axis of the furnace. The coal-air jets that collide with each other after being injected from each corner along with the stacked burners and air ports form a strong vortex in the furnace, thereby improving the mixing of coal and air.[14] In addition, the low pressure at the center of the furnace attracts coal particles and gases.[15] Most of the coal particles are burned in the furnace, and the rising flue gas transfers heat to the furnace wall and tube bundles, such as SHs, RHs, and the economizer. Some coal particles escape from the boiler without being completely burned.

Figure 3b shows the arrangement of the coal burners and air injection nozzles in the boiler. The burner system uses a coal separator that aerodynamically divides the primary air (PA) and coal into two streams—one fuel-rich and the other fuel-lean. Thus, NO_x emissions are reduced by controlling the local stoichiometric ratio (SR) in the near-burner zone.[16] The pulverized coal transported by PA is injected at a ratio of 7:3 from the concentrated and weak coal burners to create the fuel-rich and fuel-lean zones. Secondary air (SA) is supplied from the outer rim of the concentrated and weak coal burners, auxiliary air ports, oil ports, and OFAs.

The SHs, RHs, and Economizer are composed of tubes with diameters between 38 and 60.3 mm. These tube bundles are densely arranged inside the convective pass in which the transverse pitch ranges from 110 to 880 mm and the longitudinal pitch from 55 to 120 mm. Considering this geometry, creating a grid would involve a high computational cost. Therefore, these tube bundles are often assumed to be very thin or to have zero-thickness wall boundaries or are expressed as momentum and energy source terms by using a user-defined function (UDF). Accordingly, in this study, the geometry of the tube bundles was not considered by applying the UDF code.

2.2. Boiler Operating Conditions. For boundary conditions to be used in the simulation, operational data for Boryeong Power Plant Unit 3 on specific dates were collected to determine the coal and air supply conditions. The boiler exhibited an output of 554 MW with a coal supply of 209 t/h. Table 1 shows the proximate and ultimate analysis results of the coal used in the simulation. The coal burners were used at levels A to E, and the ratio of the coal distributed to the concentrated and weak coal burners was assumed to be 7:3. The combustion air was divided into PA and SA, with PA accounting for 24.3%. In addition, PA was observed at 350 K and SA at 399 K. The airflow

https://doi.org/10.1021/acsomega.1c04574
ACS Omega 2021, 6, 31132−31146

rate of each port in the boiler was adjusted by opening the damper. In this study, the airflow rate supplied from each port was calculated based on the damper opening and outlet areas. Boryeong Unit 3 operates at an overall SR of 1.15 and reduces NO_x through multiple air-staging. Coal burners, such as the concentrated or weak coal burners, PA ports, and the surrounding SA ports, are separated for air-staging at the unit burner level. Moreover, as described in the boiler specifications, the supply of coal particles from a pulverizer to the separate concentrated and weak coal burners locally control the coal-air SR in the near-burner zone. Even in one windbox (WB), the SR is adjusted according to the elevation through air distribution control. Figure 4 shows the airflow rate with furnace height to

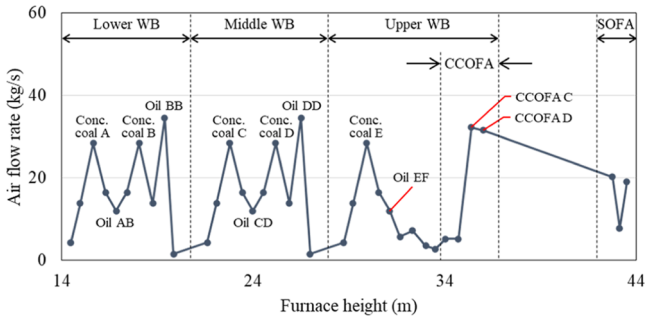

Figure 4. Airflow rate supplied by each air port with furnace height. Conc.: concentrated, CCOFA: close-coupled overfire air, SOFA: separated overfire air, and WB: windbox.

illustrate the air distribution pattern in the furnace. In the lower WB, a substantial amount of air was supplied with coal particles from concentrated burner A or burner B, but the local SR of the fuel−air mixture supplied from the burners was 0.44. Although two auxiliary air ports and one oil port AB are positioned between burners A and B, their airflow rates are low. Instead, oil port BB, located above burners A and B, supplies air at the highest flow rate to burn coal particles from burners A and B. The SR in the region below the oil port BB was 0.69, and that of the lower WB region was 0.88. Thus, in the WB, air-staging was also adopted by controlling the damper of each air port, which follows the same principle as overfire air. Moreover, the middle WB had the same pattern as the lower WB. Otherwise, in the upper WB, coal burner F is in a standby mode and supplies only a small amount of air without coal. In addition, there is no oil port above burner F but CCOFA C and D supply air at a high flow rate. The SOFA, which is installed at the top of the furnace, supplies additional air to complete the fuel combustion and maintains the overall SR of the boiler at 1.15.

3. METHODS

3.1. Boiler Mesh. The boiler mesh was mainly composed of hexahedral cells to increase computational efficiency, and tetrahedral cells were used only for small regions, as shown in Figure 5a. Most of the mesh cells were used to represent the furnace to allow a more precise representation of the flow and combustion processes. In addition, because the burners are significantly smaller than the furnace, and coal devolatilizes within a very short period in the near-burner zone, the cells were subdivided using a mesh adaptation function. The three meshes were tested to verify if the number of cells was adequate for the boiler simulation. The numbers of cells constituting the furnace were 3.2, 6.3, and 9.1 million, respectively, for the three meshes. Figure 5b shows the gas-temperature profile as a function of the number of cells. The medium and fine meshes had similar profiles, with the largest difference being only 2%. However, the profile for the coarse mesh was considerably different from those of the other meshes. Therefore, the medium mesh was used in this study.

3.2. Computational Models. *3.2.1. General Models.* The CFD analysis was conducted using ANSYS Fluent 19.2, and the pulverized coal-combustion process was modeled using the Euler−Lagrangian approach. In the model, the continuous gas phase is treated as a continuum by solving Navier−Stokes equations in the Eulerian frame, and the dispersed phase is solved by tracking a large number of particles through the flow field. The dispersed phase particles can exchange momentum, mass, and energy with the gas phase, while particle−particle interactions are not considered. Turbulence is represented by a realizable $k-\varepsilon$ model that includes an alternative formulation for the turbulent viscosity and a modified transport equation for the dissipation rate. The realizable $k-\varepsilon$ model provides improvements over the standard model, where the flow includes strong

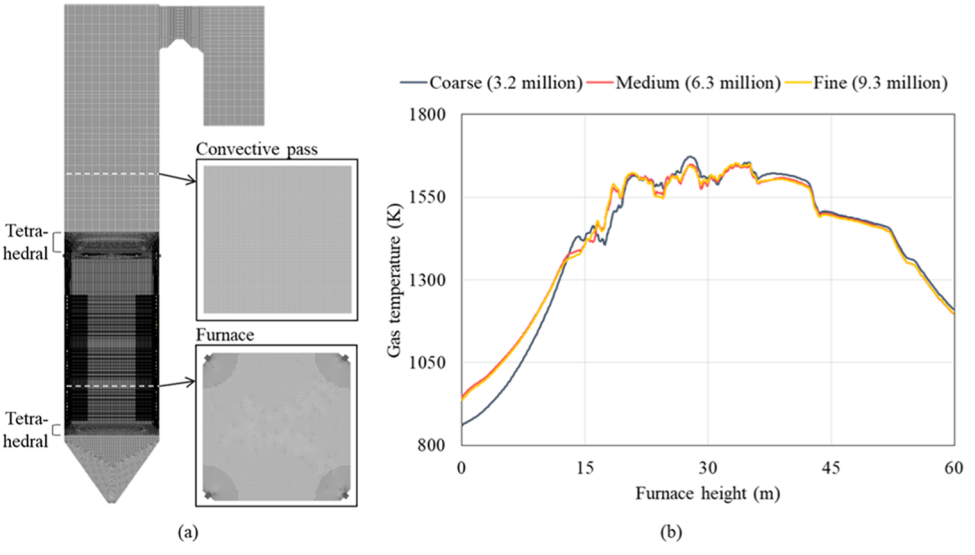

Figure 5. (a) Mesh model configuration used in the CFD and (b) the gas temperature with furnace height.

https://doi.org/10.1021/acsomega.1c04574
ACS Omega 2021, 6, 31132−31146

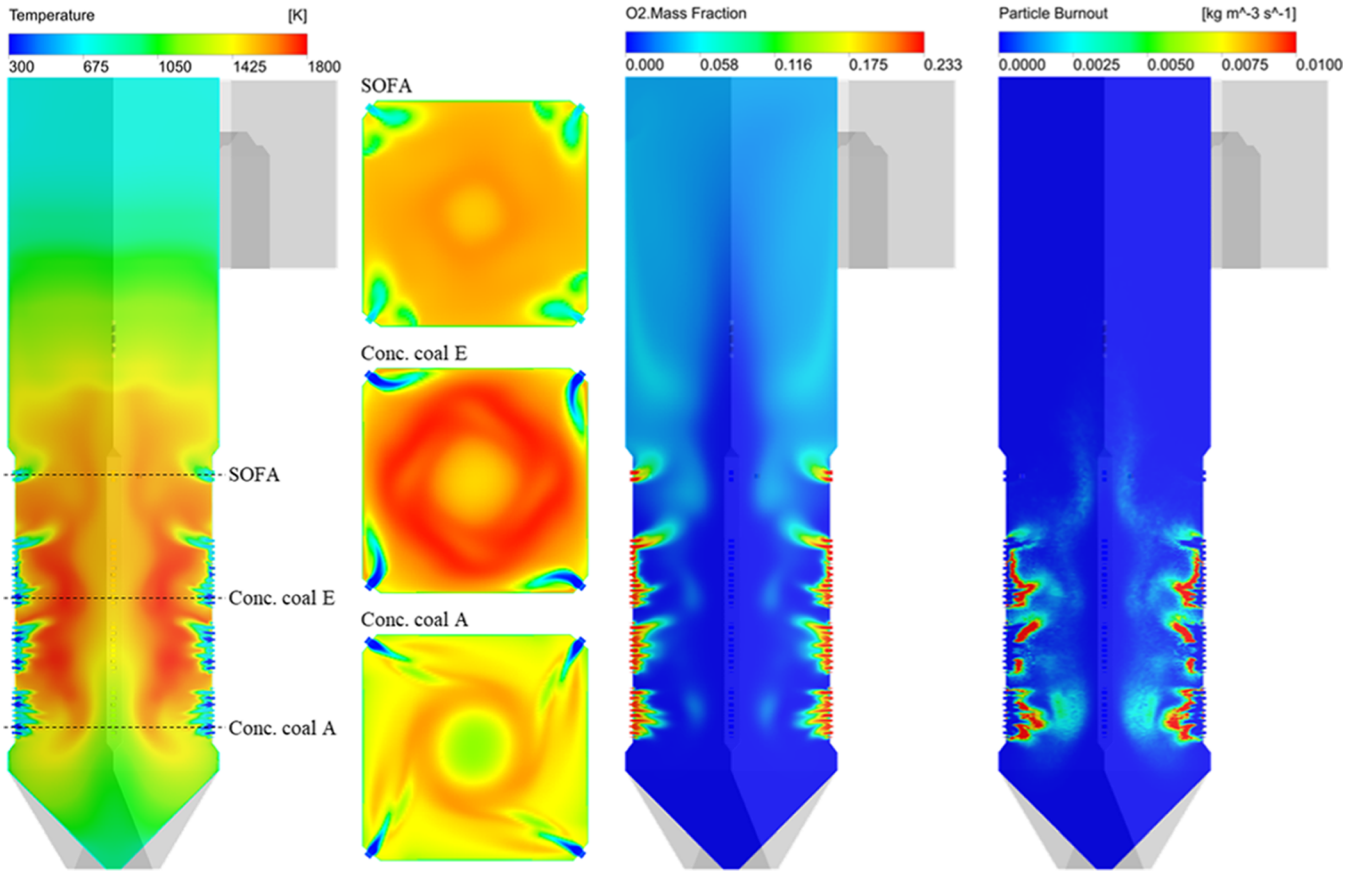

Figure 6. Contours of gas temperature, oxygen concentration, and char particle burnout.

streamline curvature, vortices, and rotation.[17] Radiation is the dominant mode of heat transfer in the furnace. In this study, the discrete ordinate model was used to represent the particle/gas-wall and particle/gas radiative transport. This model approximates the solution of the radiative transfer equation by discretizing the entire solid angle into a finite number of solid angles. The absorption coefficient of the gas mixture was calculated using the weighted-sum-of-gray-gas model, which accounts for the radiation from CO_2 and H_2O. The particle emissivity of pulverized coal depends on the fraction of unburned char;[18] however, for simplicity, the particle emissivity and scattering factor were set to 0.9 and 0.6, respectively.

3.2.2. Coal Combustion Processes. In the CFD model, the coal combustion process consists of inert heating and drying, devolatilization, volatile combustion, and char combustion, and each step is performed sequentially. In the boiler, coal particles are transported via air into the furnace and heated when exposed to a high-temperature environment. In this case, the particle temperature is determined by the thermal equilibrium between the convective heat transfer with the surrounding gas and radiative heat transfer. In the char-combustion process, a portion of the combustion heat is directly utilized for particle heating. Devolatilization begins when the particle temperature reaches 400 K after drying. The released volatile matter oxidizes to generate CO_2, H_2O, N_2, and SO_2. After complete devolatilization, the remaining char reacts with oxygen to generate CO and CO_2.

Devolatilization of coal was predicted using a single kinetic rate model with the default kinetic parameters in Fluent software. The combustion process of the char particles was predicted using the carbon burnout kinetic model.[19,20] This model calculates the char-combustion rate using a single-film char oxidation submodel. The kinetic parameters are predicted by the rank-dependent correlations.[21] In addition, the carbon burnout kinetic model consists of submodels for statistical variations in single-particle reactivity and density, thermal annealing, and physical properties. The reduction in the particle mass during devolatilization and char combustion is shown in Appendix 1. A finite-rate/eddy-dissipation model was used to calculate the homogeneous reactions of the gas phase based on turbulence-chemistry interactions. The net reaction rate was determined using the minimum value of the two reaction rates.[22]

3.2.3. Heat Transfer of the Furnace Water Wall and Tube Bundles in the Convective Pass. The heat transfer for the boiler water wall was considered to be the thermal wall boundary condition. Therefore, 653 K, which is the average steam temperature of the water wall, was set as the external temperature, and the convective heat transfer coefficient was assumed to be 500 W/(m^2 K). In addition, 0.85 was used as internal emissivity. The actual water wall steam flows from the bottom to the top, and its temperature increases through heat absorption. The heat transfer coefficient depends on the fire-side local Reynolds number and Prandtl number. In a coal boiler, ash is deposited on the inner wall during operation, which changes the internal emissivity and heat transfer coefficient. To avoid such complexity, the external heat transfer coefficient and internal emissivity were assumed to be constants.[23] The heat transfer from the gas to the tube bundles was applied as a source term for the cell zone through the UDF. The equations for the

https://doi.org/10.1021/acsomega.1c04574
ACS Omega 2021, 6, 31132−31146

convective[24,25] and radiative[26] heat transfer coefficients are given in Appendix 2.

3.2.4. NO_x Formation and Reduction. The NO_x generation and reduction processes were modeled through postprocessing after calculating the flow, temperature, and species concentration. The NO_x model included fuel NO_x and thermal NO_x; thermal NO_x was predicted using the extended Zeldovich mechanism.[27] Fuel-N was divided into volatile-N and char-N. The ratio at which volatile-N was converted into HCN and NH_3 was set to 9:1. Volatile-N is mostly converted to HCN for high-rank fuels, such as bituminous coal,[22] and char-N is directly converted to NO. Some of the formed NO was reduced to N_2 through a surface reaction with the char particles. This is an adsorption reaction, proportional to the specific surface area of the pores on the particle surface. For the Brunauer–Emmett–Teller (BET) specific surface area of the coal particles, 25 000 m^2/kg was used as the default value in Fluent software. NO reduction by reburning was predicted using a partial equilibrium model.[29] The detailed reactions are provided in Appendix 3.

4. RESULTS AND DISCUSSION

4.1. Base Case Results and Their Validation. The simulation was conducted based on the operating conditions of Boryeong Unit 3, and the model was verified through a comparison with the actual measurements at the boiler site. In addition, the position of the methane gas nozzle was evaluated based on the simulation results. Figure 6 shows the gas temperature, oxygen mole fraction, and char burnout inside the boiler. The coal–air mixture was injected from the corners burned with a strong vortex, thereby forming a fireball with a circular flame cross section. In this case, the flame temperature was higher in the middle or upper WB than in the lower WB. The temperature contours from the top view of the furnace show that the peak temperature of the fireball and the average gas temperature were significantly higher at the upper level of burner E than burner A. In addition, at the SOFA section, the fireball shape became blurred, and even temperature distribution was observed. As the oxygen supplied from each port was rapidly consumed through the combustion of coal, oxygen was deficient near the fireball. Above the CCOFA C and D, the oxygen mole fraction was high because a large amount of air was supplied. Coal particles burned most actively near the burners, and some exhibited continuous combustion up to the top of the SOFA section.

Table 2 shows the gas temperature, oxygen concentration, unburned char, and NO_x concentration at the boiler outlet of Boryeong Unit 3 and the simulation results. For all of the variables, the simulation results exhibited an error of less than 5%, confirming high accuracy. For reference, the boiler NO_x emissions in a power plant are often converted into values when the oxygen content in the flue gas is 6%. Figure 7 shows a comparison of the heat absorption of the furnace water wall and each tube bundle in the convective pass. Although some errors were observed, heat absorption was predicted within an error range of less than 5% in all cases. In addition, the simulation results followed the heat absorption tendency of each heat exchanger. The simulation predicted the total heat absorption to be approximately 1% lower than the measured value. Although no comparison could be made for the inside of the furnace, especially near the flame because of the absence of measuring instruments, it was confirmed that the simulation accurately predicted the boiler outlet results and heat adsorption.

Table 2. Comparison of the CFD Simulation Results at the Boiler Outlet and Measured Values at Boryeong Unit 3

	gas temperature (K)	O_2 mole fraction (%)	unburned char (%)	NO_x (ppm, 6% O_2 content)
Boryeong Unit 3	624.7	3.18	5.22	118.6
CFD	629.3	3.05	5.03	121.9

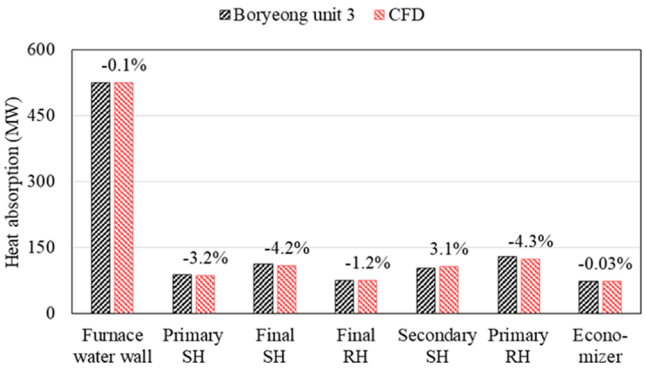

Figure 7. Heat absorption and error for the furnace wall and each tube bundle.

A postprocessing calculation was performed by applying the NO_x model to the simulation results of Boryeong Unit 3, as shown in Figure 8. The NO mole fraction was dependent on the gas-temperature distribution and was, therefore, highest at the fireball surface. In contrast, negligible levels of NO_x were observed inside the fireball even though the temperature was approximately 1500 K. This is because oxygen did not exist in this zone and fuel NO_x was not formed inside the fireball as coal particles were burned near the burners or along the outer surface of the fireball.

Figure 8a shows the NO formation and reduction rates; the regions near the burners are very dark brown indicating that fuel-N was converted to NO. In the model, char-N was directly converted into NO, which caused a high NO formation rate where char particles were burned. During devolatilization prior to the char-combustion process, volatile N was emitted as HCN and NH_3, which could be converted to NO or N_2 depending on the oxygen concentration. Devolatilization, however, is a process that is completed within a very short time immediately near the burners, where the oxygen fraction is high. Thus, the rate of volatile-N conversion to NO is also high near the burners. Therefore, the NO formation rate was high near the burners because of the influence of volatile-N and char-N. As the distance from the burners increased, some of the NO was reduced again owing to the deficiency of oxygen (appearing in blue in the contours). Therefore, in Figure 8, the outside of the fireball appears brown and the inside as blue. Most of the NO actively reacted below the CCOFA section. At the top of the SOFA section, the NO reaction zone was seen because of the slight combustion of the unburned char. After primary SH, NO hardly reacted because the gas temperature decreased and most of the char particles had already been burned.

Figure 9 shows the average NO mole fraction and NO rate with furnace height. The NO mole fraction was low in the hopper at the bottom of the furnace but gradually increased as the furnace height increased. The NO mole fraction was highest at the end of the middle WB, after which the NO mole fraction decreased because burner F did not supply coal, and the nearby

https://doi.org/10.1021/acsomega.1c04574
ACS Omega 2021, 6, 31132–31146

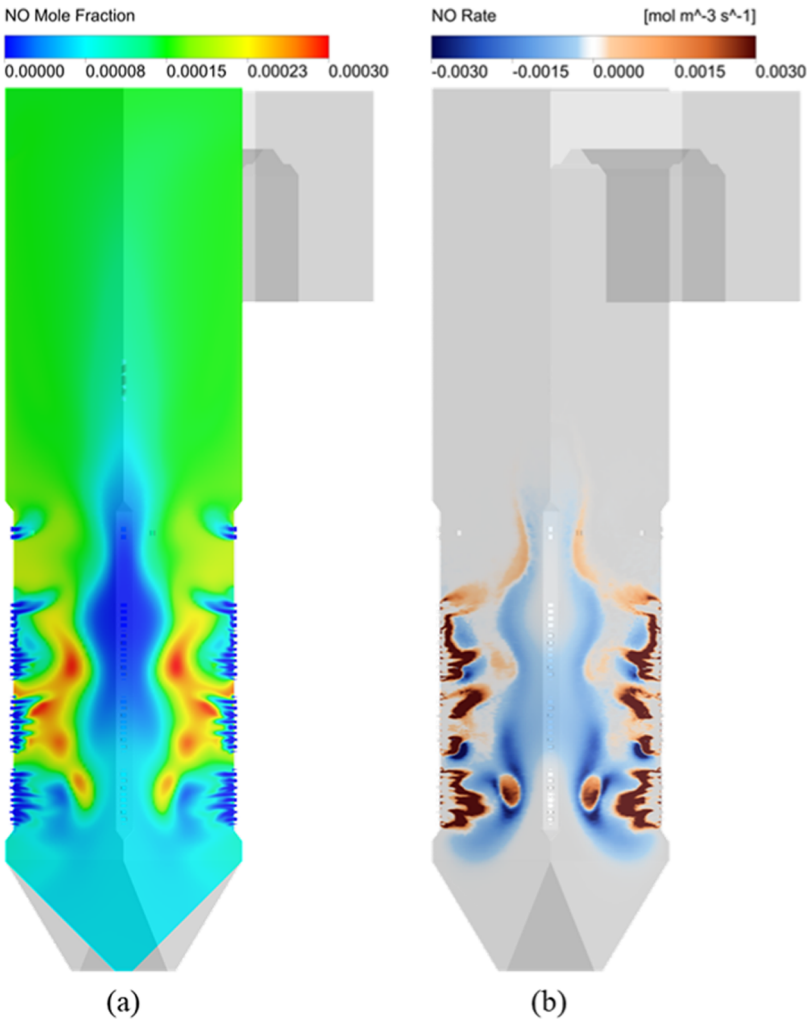

Figure 8. Contours of the (a) NO mole fraction and (b) NO rate. NO formation is shown in brown and reductions in blue; NO rates close to zero are transparent.

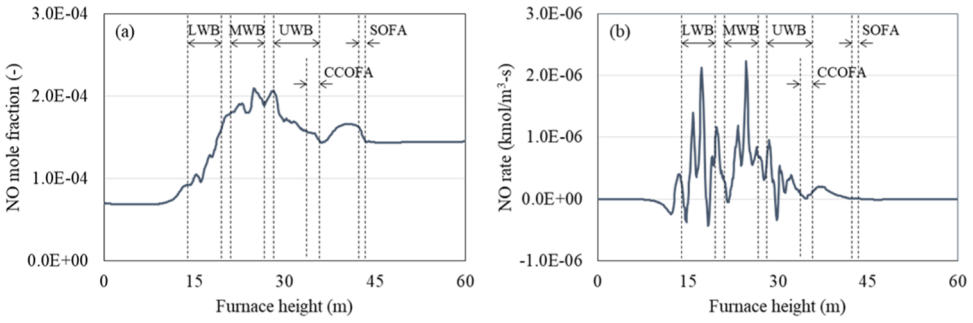

Figure 9. (a) NO mole fraction and (b) NO rate as a function of furnace height. LWB: lower windbox, MWB: middle windbox, and UWB: upper windbox.

air ports supplied a small amount of air. At the top of the CCOFA C and D, the NO mole fraction slightly increased due to the high airflow rate but decreased again due to dilution with SOFA. Figure 9b shows that NO forms mainly in the lower and middle WBs. In addition, the NO rate was almost zero after the SOFA section.

The spatial distribution of NO inside the furnace is shown using the iso-volume function in Figure 10. NO was present throughout the entire furnace, but the display condition was set to NO mole fraction > 0.0002 to visualize the main NO stream. The plane in the iso-volume (at the elevation of oil port EF) also showed the NO mole fraction, but it is shown again to aid interpretation. In the region above the plane, NO rose from each corner of the furnace as it turned along the surface of the fireball. Therefore, if oil port EF is selected as the injection position, methane would be injected into the region with a high NO concentration and, thus, NO would be adequately reduced by the reburning mechanism.

4.2. Optimal Positioning of the Methane Gas Injector.

In conventional reburning, the SR of the primary combustion

https://doi.org/10.1021/acsomega.1c04574
ACS Omega 2021, 6, 31132−31146

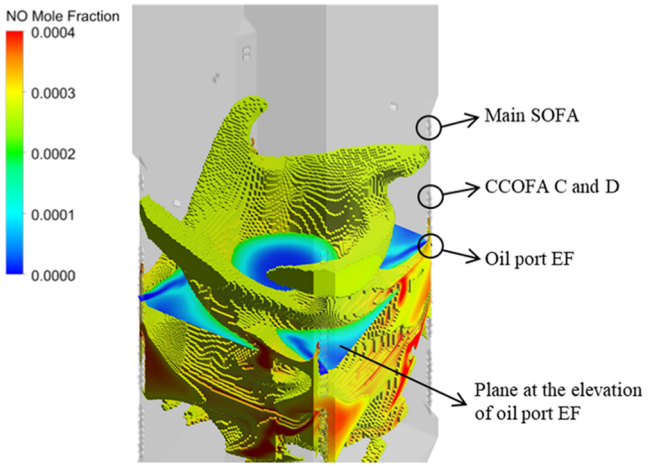

Figure 10. Spatial distribution of NO inside the furnace.

zone is between 1.10 and 1.15, implying that most of the primary fuel contained in the flue gas is burned out before reaching the reburning zone. In Boryeong Unit 3, as shown in Figure 11, the

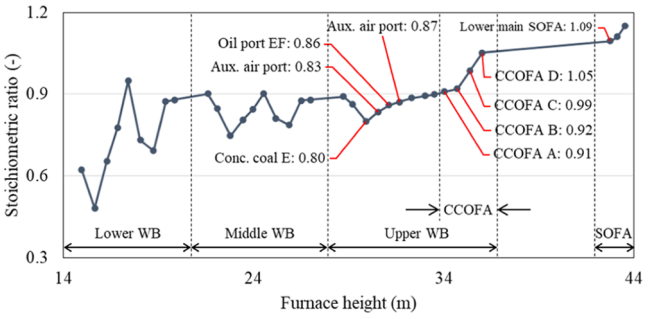

Figure 11. Stoichiometric ratio with furnace height.

SR was greater than 1.10 at the SOFA section, which contains the uppermost air ports in the furnace. A substoichiometric condition was maintained even below the CCOFA D to reduce fuel-NO_x formation. According to the conventional reburning configuration, the reburning fuel injector should be installed above the CCOFA D. However, in this study, the methane injector must be located in the existing air ports to avoid modification of the furnace wall. The possible options are auxiliary air ports, oil port EF, and CCOFAs above the coal burner E. Thus, regardless of the methane injector location, the primary combustion zone must be substoichiometric, unlike the conventional reburning configuration.

The lower the position of the installed methane injectors, the longer the methane residence time, and the higher the reduced NO_x emissions. However, this reduces the SR of the primary combustion zone and, thus, more unburned coal particles must compete with methane for oxygen. As methane is generally more combustible than coal, cofiring might hinder coal combustion. However, if most of the fuels can be burned in the burnout zone, methane injectors at a lower level can effectively reduce NO_x emissions. Therefore, in this study, oil port EF was set as the methane injector location, whereas the lowest air port above the burner E served as the auxiliary air port. However, the advantage of positioning the oil port EF directly above is the ability to replace the start-up fuel with methane with no significant difference in the methane residence time. Accordingly, the SR of the primary combustion zone was 0.83 when the oil port EF served as the methane injection location. As shown in Figure 4, the low flow rate at the air ports from the oil port EF to the CCOFA B will promote NO_x reduction by reburning in this region.

In this study, the effects of methane cofiring rate up to 40% were evaluated. Methane injection nozzles with a 6 in. diameter were created in the center of the oil port EF at each corner in the existing boiler geometry. The gas temperature was set to 300 K, and the injection speed was in the range of 54.7−218.8 m/s. This is the typical speed range for gas reburning.[9] As the methane nozzle was very small with respect to the scale of the boiler, a square was assumed with the same area to facilitate meshing. In Figure 12, the yellow square inside the oil port EF indicates the methane gas nozzle.

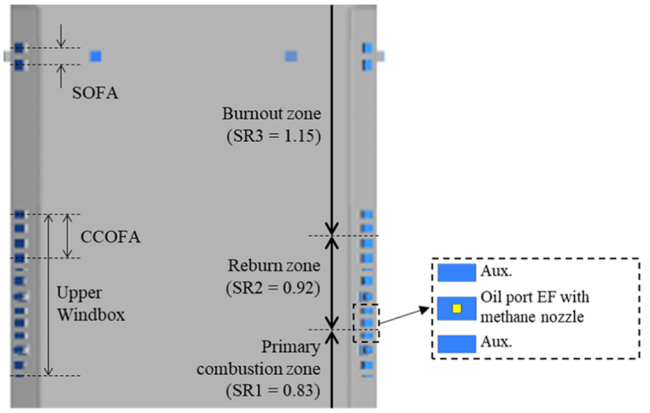

Figure 12. Location of the methane gas injection nozzle (yellow square) and the stoichiometric ratio in each zone.

As the methane input increased, the coal feed rate decreased in the primary combustion zone to maintain the total heat input in the boiler. The amount of air supplied in the primary combustion zone also decreased to maintain SR1 at 0.83. Otherwise, the flue gas NO_x level entering the reburning zone will increase, which can be difficult to control with gas reburning. In the reburning zone, the injection of methane fuel decreased SR2 from 0.92 (the existing operating condition) to 0.59. The air for methane combustion was supplied through the CCOFA C to the SOFA section in the burnout zone; it was not supplied in the reburning zone to ensure an adequately high methane residence time. In all cases, the overall stoichiometric ratio SR3 was fixed at 1.15. First, simulation was performed to predict the NO_x distribution inside the coal boiler. Next, case studies were conducted to determine the effects of methane cofiring, including NO_x emission characteristics. The SR for each case is shown in Table 3.

4.3. Effects of Methane Cofiring Rates. Figure 13 shows the gas temperature and char particle oxidation with furnace height under methane gas cofiring. An increase in the methane cofiring rate decreased the gas temperature in the primary

Table 3. Stoichiometric Ratios in the CFD Cases

methane cofiring rate (%)	SR1	SR2	SR3
0 (base)	0.83	0.92	1.15
10		0.84	
20		0.76	
30		0.67	
40		0.59	

https://doi.org/10.1021/acsomega.1c04574
ACS Omega 2021, 6, 31132−31146

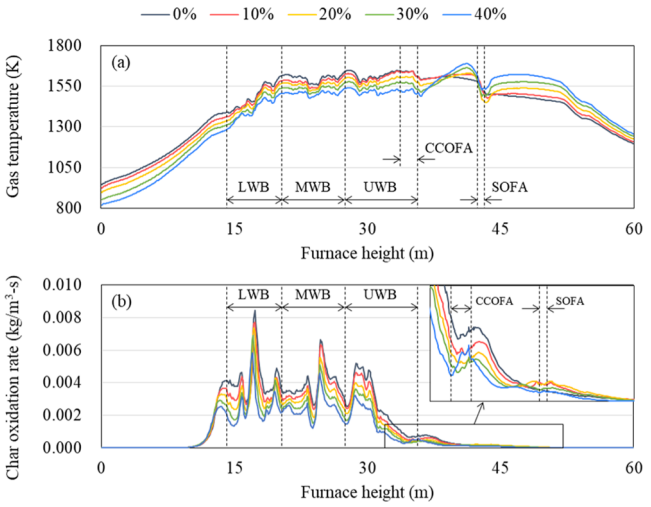

Figure 13. (a) Gas temperature and (b) char oxidation with furnace height as a function of the methane cofiring rate.

combustion and reburning zone. The gas temperature, which was significantly low at a high cofiring rate, increased sharply above the CCOFA section. Methane was not significantly oxidized under the low SR of the reburning zone, whereas it reacted rapidly with CCOFA to increase the low flue gas temperature. Eventually, the cofiring rate and the gas temperature became positively correlated above 38.5 m; thus, the thermal load was shifted upward. This relationship was evident even above the SOFA section, suggesting that methane cofiring can overheat the tube bundles, especially that of the primary SH. According to the simulation results, the flue gas temperature entering the primary SH increased by approximately 30 K per 10% of the cofiring rate.

Figure 13b shows the char particle oxidation rate. The decrease in the coal feed rate due to the increase in the methane cofiring rate represented a clear cause of the variations in the char oxidation rate profile, with no changes in this pattern observed, with the exception of the upper furnace. When the methane gas was supplied, the char oxidation rate at the SOFA section was higher than that of the base case. As the methane gas consumed oxygen faster than that by char, the combustion of a portion of the char particles is delayed until they reach the SOFA section.

However, char oxidation at the SOFA section was reduced at the cofiring rate of 30% and was significantly lower than that of the base case at the cofiring rate of 40% due to the high velocity of CCOFA. In the 40% case, as the reburning zone, SR was reduced to 0.59 and the flow rates of the CCOFA and SOFA were significantly increased to maintain the overall SR. Thus, CCOFA was injected at a high velocity, which promoted combustibility by improving the mixing of char particles and air. Therefore, the unburned char at the boiler outlet with methane cofiring was in the 4.90−4.94% range, which did not differ significantly from that in the base. Although char combustion could be hindered by methane, the high flow rates of CCOFA and SOFA prevented the unburned char from venting to the boiler outlet.

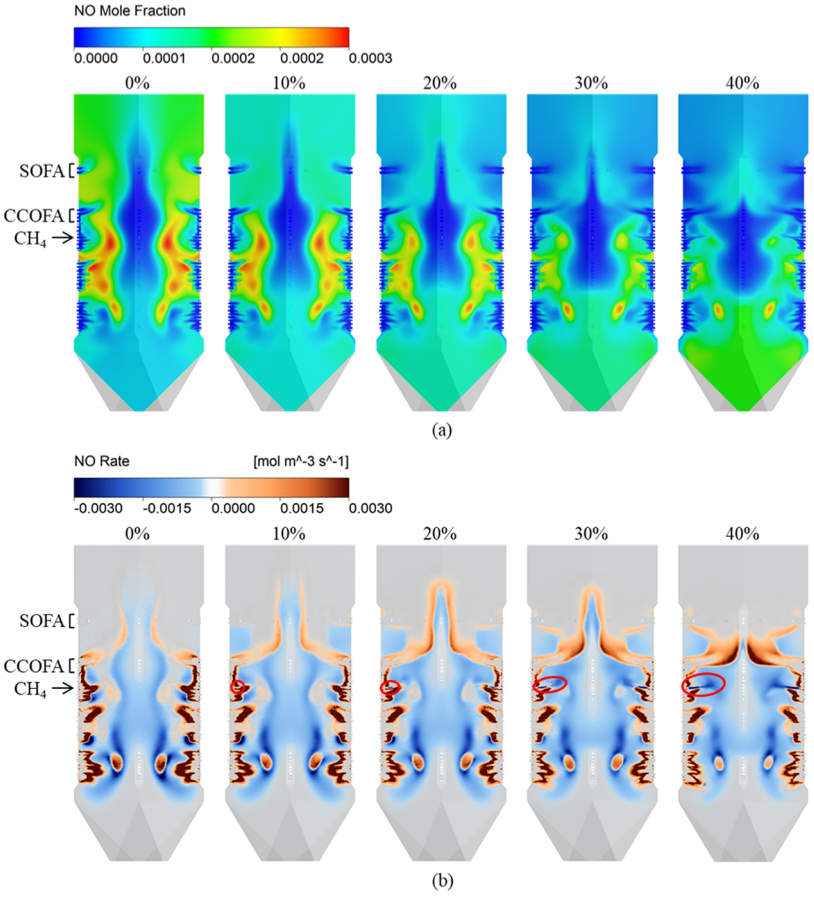

Figure 14. Contours of the (a) NO mole fraction and (b) NO rate as a function of the methane cofiring rate.

https://doi.org/10.1021/acsomega.1c04574
ACS Omega 2021, 6, 31132−31146

Figure 14 shows the contours of NO mole fraction and NO rate inside the furnace according to the methane cofiring rate. The reduced coal feed and the low gas temperature in the primary combustion zone during methane cofiring resulted in a decrease in the NO mole fraction near the fireball. As the cofiring rate increased, the NO gradually disappeared. The methane cofiring rate and the NO mole fraction were negatively correlated even at the upper portion of the furnace due to the low SR and NO_x destruction by hydrocarbon radicals in the reburning zone.

In the NO rate results in Figure 14, the red lines represent the NO_x reduction zone due to the reburning mechanism. The NO_x reduction (blue) appears as a small dot near the burner in the 10% case, and however, extends to the outer surface of the fireball in the 30 and 40% cases. The high cofiring rate facilitated the penetration of methane to the furnace center, which further reduced NO_x. In contrast, when the cofiring rate increased, the brown color in the upper furnace gradually became darker, that is, more NO was produced. However, the NO reduction reaction was dominant as the NO mole fraction at the furnace top, which is directly related to boiler emissions, was negatively correlated with the cofiring rate. Additionally, in the 40% case, a low amount of NO was produced at the top of the SOFA section, unlike the other cases. This resulted from the high-velocity CCOFA burning of most of the char, as previously described in Figure 13.

Figure 15 shows the NO mole fraction and NO rate profiles with the furnace height. The NO mole fraction in the burner

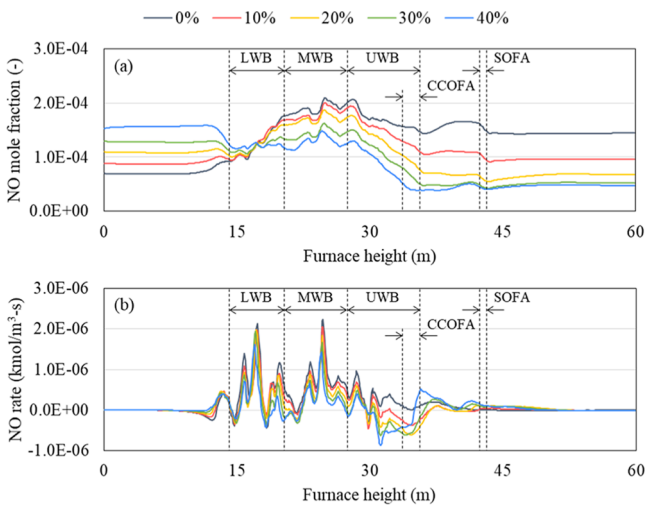

Figure 15. (a) NO mole fraction and (b) the NO rate with furnace height as a function of the methane cofiring rate.

zone decreased with an increase in the cofiring rate, which was highly evident at the top of the furnace. The NO mole fraction, which was 144 ppm in the base case, decreased to 48−97 ppm when methane cofiring was applied. However, the reduction of NO_x emissions by methane cofiring was limited, that is, the NO_x reduction rate per methane input decreased as the cofiring rate increased. By comparing the 30 and 40% cases, little difference was observed in the NO mole fraction above the SOFA section. The increase in the NO mole fraction above the CCOFA section in the 40% case suggested that high airflow rates of the CCOFA and SOFA could increase the NO formation.

The NO rate in Figure 15 indicates that the NO reduction was proportional to the cofiring rate in the reburning zone (between a height of 31 m and the CCOFA section). NO formation increased at the SOFA or both CCOFA and SOFA sections with methane cofiring, of which the effect on emission generation was less than that on the reduction reaction in the reburning zone. Consequently, the NO_x emissions of 36.9 ppm (at 6% O_2) were achieved at the boiler outlet in the 40% case, which is a decrease of 69.8% from that of the base case.

Figure 16 shows the spatial distribution of methane gas for different cofiring rates, with NO reduction rate, via the reburning mechanism, represented by the colored sections. Methane was present in a narrow area near the furnace walls in the 10% case; as the cofiring rate increased, it penetrated the furnace center and occupied a wide area. The methane swirled up along the fireball and was primarily oxidized over the SOFA section. The NO reduction rate by reburning was highest near the injector and gradually decreased toward the top. As methane was already widely distributed in the furnace within the 30% case, it may be difficult to further increase the NO_x reduction rate even if the cofiring rate is increased.

Figure 17 presents the NO mole fraction profile and its influencing factors above 30 m, as the methane injectors are located at 31 m. As shown in Figure 17a, in the 0% case, the very low airflow rate from the oil port EF to the CCOFA B in the upper WB formed a reducing condition; therefore, the NO mole fraction gradually decreased with the increase in height. Above the CCOFA section, NO increased due to residual char combustion, decreased again by SOFA dilution, and subsequently, remained constant. At a height of 30 m, just below the methane injectors, the NO concentration in the flue gas from the primary combustion zone was 170 ppm. With the methane cofiring, the NO concentrations were found to be 157, 142, 122, and 106 ppm corresponding to 92.3, 83.4, 71.7, and 62.2%, respectively, of that in the base case. As the SR of the primary combustion zone remained constant in all cases, the primary NO levels in each case were determined by the fuel-N input on replacing coal with methane. As the cofiring rate increased, the slope of the NO mole fraction in the upper WB became steeper, which was explained by NO destruction by CH radicals and the low SR in the reburning zone.

Figure 17b shows the NO destruction by CH radicals, i.e., the reburning NO rate. It was highest at the proposed location of methane injectors (31 m) and gradually decreased as the height increased. In the NO_x model, the reburning NO rate was positively correlated with the concentrations of CH_4 and NO and the gas temperature. However, the NO concentration and gas temperature did not directly influence the reburning NO rate. As the cofiring rate increased, the local NO concentration decreased across the reburning and burnout zones. In addition, with the methane cofiring, the NO mole fraction and temperature of the flue gas entering the reburning zone were also lower than those of the base case. Therefore, this confirmed that the reburning NO rate was mainly dominated by the methane mole fraction.

Methane cofiring, which is sensitive to the fuel-NO_x formation, required the adjustment of air supply conditions. Therefore, to determine the net effect of reburning on NO_x emissions, the NO_x reduction caused by the change in operating conditions must be separated. As shown in Figure 17f, with methane cofiring, the low SR of the reburning zone reduced the fuel NO rate by creating a reducing atmosphere below the CCOFA section. In contrast, between the CCOFA and SOFA sections, the fuel NO rate significantly increased even though the char oxidation rate was lower than that of the base case. This

https://doi.org/10.1021/acsomega.1c04574
ACS Omega 2021, 6, 31132−31146

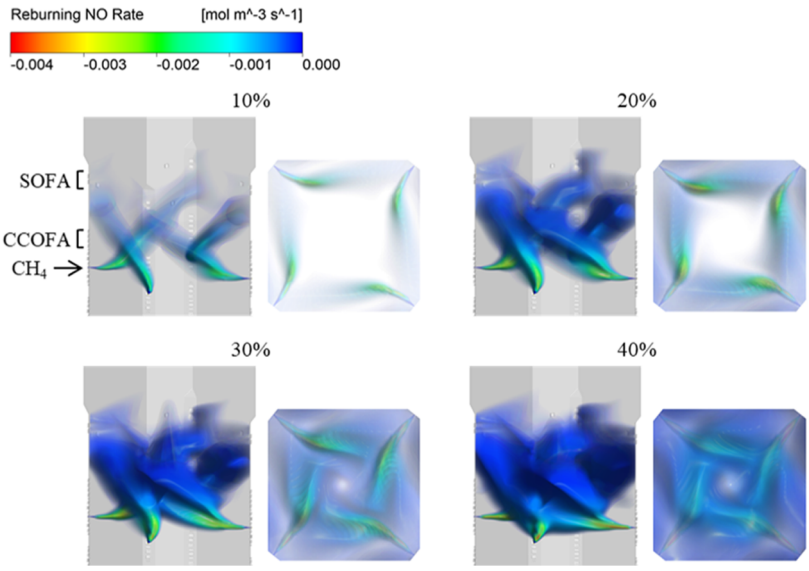

Figure 16. Spatial distribution of CH_4 as a function of the methane cofiring rate, with colored parts showing the reburning NO rate.

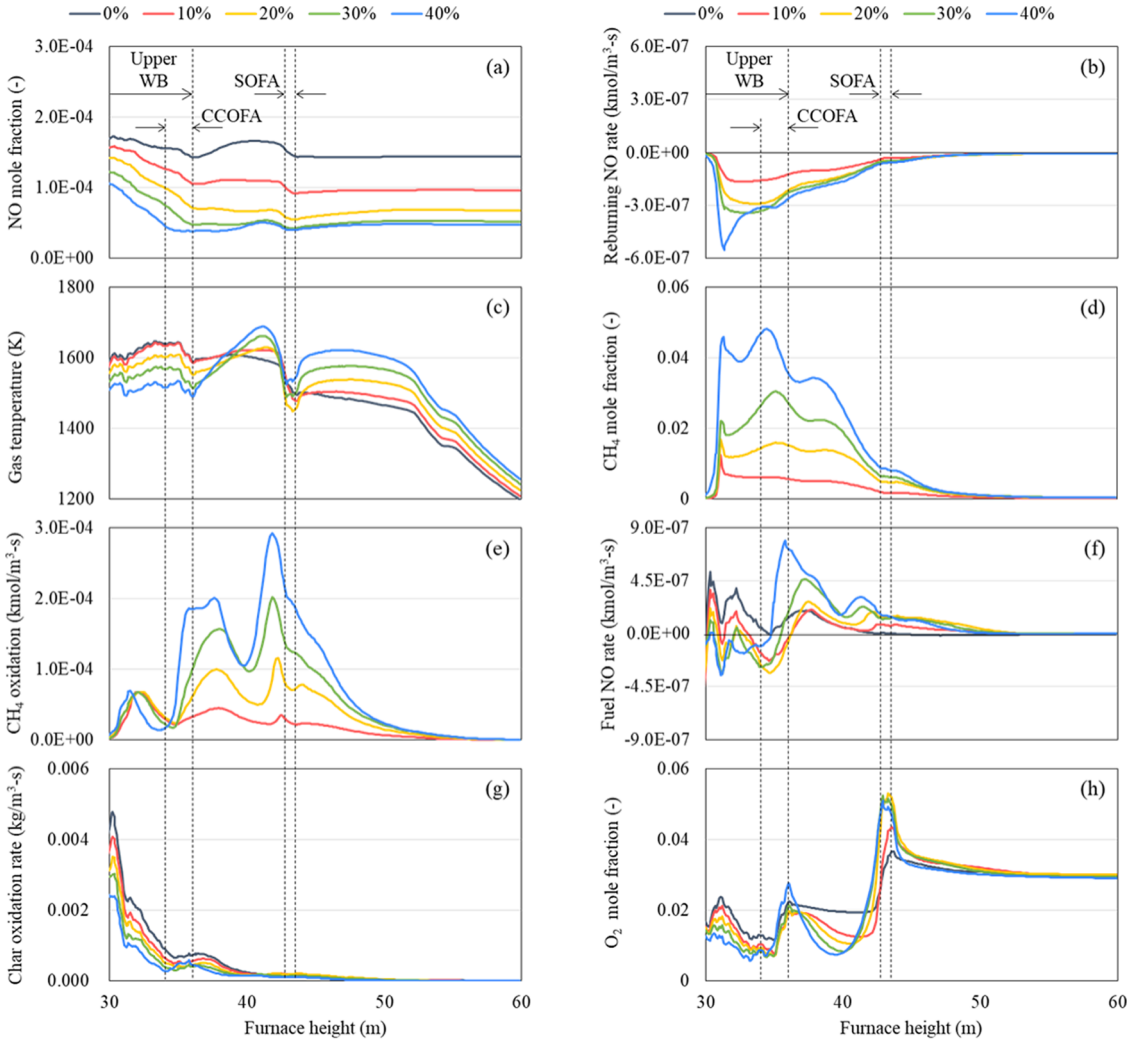

Figure 17. Profiles of (a) the NO mole fraction and influencing factors on NO: (b) NO reduction by reburning, (c) gas temperature, (d) CH_4 mole fraction, (e) CH_4 oxidation, (f) fuel NO rate, (g) char oxidation rate, and (h) O_2 mole fraction.

increment could be due to the local oxygen mole fraction. Below the SOFA section, the average oxygen mole fraction along the furnace height was inversely proportional to the cofiring rate. However, the high flow rates of the CCOFA and SOFA caused

https://doi.org/10.1021/acsomega.1c04574
ACS Omega 2021, 6, 31132−31146

by methane cofiring created a local fuel-lean condition, which resulted in an increase in the fuel NO formation. Additionally, the production of thermal NO_x was much less than that of fuel NO_x, even with an increased methane input.

With methane cofiring, the decrease in the char oxidation rate was caused not only by the reduced coal feed but also by the lower SR in the upper WB and increased oxygen starvation due to methane combustion. However, the application of methane cofiring did not increase the unburned char emissions at the boiler outlet because char combustion was promoted by the CCOFA and SOFA. Methane started to oxidize immediately after injection and most of it was also burned out by the CCOFA and SOFA. Although weak, the combustion of methane gas continued up to approximately 52 m, the height at which the primary SH was located. Therefore, the SR of the reburning zone should be increased to ensure tube safety.

4.4. Assessments to Determine the Optimal Methane Cofiring Rate. The NO_x emissions at the boiler outlet, fuel loss, and the furnace exit gas temperature (FEGT) were evaluated to determine the optimum methane cofiring rate in the boiler. Figure 18 shows the normalized NO_x emissions and the

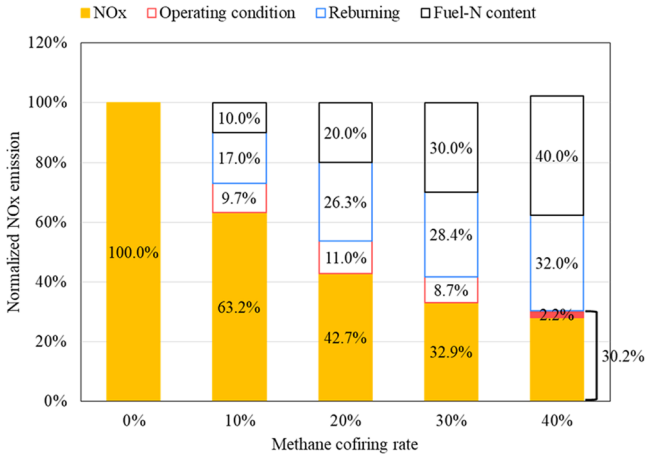

Figure 18. Normalized NO_x emissions and reductions according to different factors, as a function of the methane cofiring rate.

contributions to NO_x reduction according to different factors. "NO_x" refers to the percentage of NO_x emitted at the boiler outlet in each case. The "reburning" NO_x reduction was obtained by integrating the rate at which NO was reduced to HCN or CN in the total boiler volume, which corresponded to 17.0, 26.3, 28.4, and 32.0% of NO emissions in the base case for the methane cofiring rates of 10, 20, 30, and 40%, respectively. "Fuel-N content" is the nitrogen reduction effect achieved by replacing coal with methane, which is the same as the methane cofiring rate. The "operating condition" in Figure 18 refers to the reduction of fuel NO_x due to the change in the air supply condition accompanied by the application of cofiring. This value was obtained by subtracting "NO_x", "reburning", and "fuel-N content" from unity in each case. In the 10 and 20% cases, the operating condition contributed to NO_x reduction by 9.7 and 11.0%, respectively. However, it decreased to 8.7% in the 30% case and increased the NO_x formation in the 40% case. Excessively high percentages of CCOFA and SOFA caused the char particles to burn at a high local SR, increasing the fuel-NO_x formation. Through this classification, the nitrogen content of the reburning fuel was found to play an important role in NO_x reduction. In particular, in this study, the influence of the operating conditions was considerably important. Even if a higher methane cofiring rate reduces the NO_x by the reburning mechanism, the boiler NO_x emissions may eventually be limited by the air operating conditions, i.e., the SR. In addition, in boilers with already optimized operating conditions, the NO_x reduction by methane cofiring may be less than that achieved in this study.

Figure 19 shows the fuel loss and NO_x emissions according to the methane cofiring rate. The fuel loss was determined by

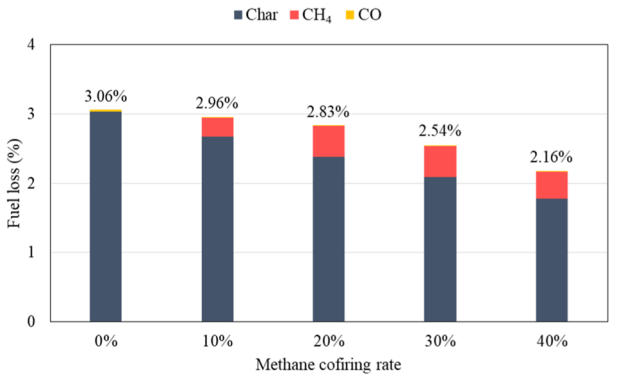

Methane cofiring rate		0%	10%	20%	30%	40%
Fuel loss (%) = Heating value of unburned fuel / Total heat input × 100%	Total	3.06	2.96	2.83	2.54	2.16
	Char	3.03	2.68	2.38	2.09	1.77
	CH_4	-	0.27	0.44	0.45	0.39
	CO	0.0245	0.0152	0.0081	0.0030	0.0005

Figure 19. Carbon-based fuel losses in the boiler as a function of the methane cofiring rate.

dividing the heating values of unburned fuels including char, methane, and CO by the total heat input. The char fuel loss decreased with the increase in the cofiring rate, which was mainly attributed to the reduced coal feed rate. The difference in the unburned char at the boiler outlet based on the cofiring rate was insignificant. The methane fuel loss increased and then decreased due to improved fuel−air mixing by the CCOFA and SOFA. Although CO was negatively correlated with the cofiring rate, its proportion in fuel loss was extremely low. However, CO emissions can be used as an indicator of flame stability. The total fuel losses were reduced by 3.3, 7.4, 16.9, and 29.3% for the cofiring rates of 10, 20, 30, and 40%, respectively. Thus, methane cofiring reduced fuel loss and CO emissions.

Although the achievable NO_x reduction was evidently limited, the high methane input rate had positive effects on NO_x reduction and fuel efficiency. When the methane input rate was increased, the primary combustion zone SR was fixed to avoid an increase in the NO_x level in the flue gas entering the reburning zone, and accordingly, the flow rates of CCOFA and SOFA were increased. Therefore, methane cofiring increased the thermal load in the upper furnace and the FEGT. Figure 20 shows the NO_x emissions at the boiler outlet and the FEGT with the methane cofiring rate. At a cofiring rate of 40%, NO_x emissions were reduced by 85 ppm, but compared to the base case, the FEGT was increased by 125 K. For the boiler used in this study, the FEGT was designed to be 1511 K, and exceeding this value might damage the steam tube material. If a high cofiring rate is required to reduce CO_2 emissions, the target FEGT may be achieved by diverting a portion of the CCOFA and SOFA to the lower air ports. However, in this case, the increased SR in the primary combustion or reburning zone can lead to increased NO_x emissions. Therefore, to apply methane

https://doi.org/10.1021/acsomega.1c04574
ACS Omega 2021, 6, 31132−31146

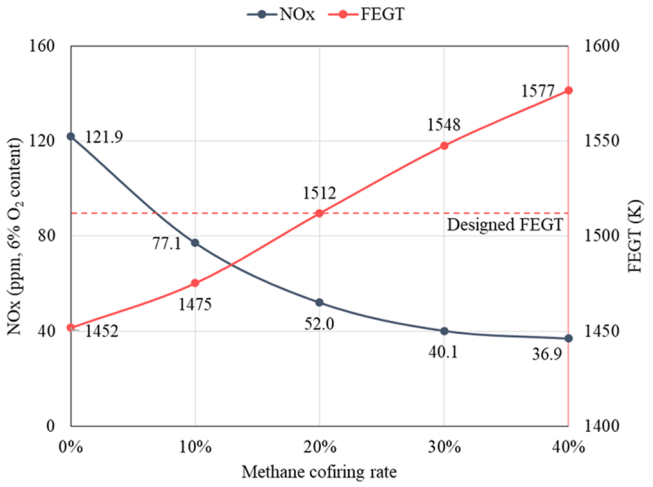

Figure 20. NO_x emissions at the boiler outlet and the furnace exit gas temperature (FEGT) as a function of the methane cofiring rate.

cofiring without modifying the tube, the determined optimal methane cofiring rate was 20%.

5. CONCLUSIONS

In this study, numerical simulations were conducted to investigate the effects of methane gas cofiring (up to 40%) on NO_x emission and combustibility in Boryeong Power Plant Unit 3, a 550 MW tangentially fired pulverized-coal boiler. Furthermore, the optimal position of the gas injection nozzle and optimal methane cofiring rate were suggested based on simulation results. The base case was validated by comparing the calculation results with the field data, which were well predicted within an error range of less than 5%. The study findings and conclusions are as follows:

(1) To determine the optimal gas injection nozzle position, SR as a function of furnace height and airflow rate was evaluated by considering the spatial distribution of NO inside the furnace. The results show that the oil port EF with a high NO environment is the optimal position for reducing NO_x emissions despite the fact that the SR of the primary combustion zone is decreased.

(2) The NO_x reduction is logarithmically proportional to the methane cofiring rate. That is, at a cofiring rate of 40%, compared to the base case, NO_x emissions are reduced by 69.8% due to reduced fuel-N caused by substituted methane and the reburning mechanism. In addition, the fuel loss decreases with increasing methane cofiring rate, implying that fuel can be consumed more effectively during cofiring.

(3) Despite these advantages of increasing methane cofiring, the 20% methane cofiring rate with a NO_x reduction of 57.3% was found to have the best performance owing to the designed FEGT value. Thus, high FEGT at 30% or a higher methane cofiring rate might damage the tube material.

APPENDIX 1: DEVOLATILIZATION AND CHAR COMBUSTION

The devolatilization of coal was predicted using a single kinetic rate model. The mass reduction of the particles during devolatilization can be expressed as follows:[22]

$$-\frac{dm_p}{dt} = k_{dev}[m_p - (1 - f_{v,0})(1 - f_{w,0})m_{p,0}] \quad (1)$$

where m_p is the particle mass, t is the time, $f_{v,0}$ is the mass fraction of volatiles, and $f_{w,0}$ is the mass fraction of the evaporating material. The subscript 0 indicates the initial condition. The kinetic rate of devolatilization, k_{dev}, is defined using an Arrhenius-type pre-exponential factor, A_{dev}, and an activation energy, E_{dev}, as follows:

$$k_{dev} = A_{dev} \exp(-E_{dev}/RT_p) \quad (2)$$

where T_p is the particle temperature and R is the gas constant.

The combustion process of the char particles was predicted using the carbon burnout kinetic model. The mass reduction of particles during char combustion is expressed as follows:[19,20]

$$\frac{dm_p}{dt} = -A_p q = -A_p k_{char} P_s^n \quad (3)$$

where A_p is the particle external surface area, q is the global oxidation rate of the char per unit external surface area, P_s is the partial pressure of oxygen at the particle surface, and n is the global reaction order. The temperature-dependent rate coefficient, k_{char}, is expressed as follows:

$$k_{char} = A_{char} \exp(-E_{char}/RT_p) \quad (4)$$

where A_{char} and E_{char} are the pre-exponential factor and the activation energy for the oxidation of char, respectively. P_s in eq 3 can be derived using the transport model. Moreover, q is expressed as follows:

$$q = \frac{k_d}{\gamma} \ln\left[\frac{1 - \gamma P_s/P}{1 - \gamma P_g/P}\right] \quad (5)$$

where P is the total pressure and P_g is the ambient oxygen partial pressure. The mass transfer coefficient, k_d, is expressed as follows:

$$k_d = \frac{M_C D_{ox} Sh}{d_p R T_m \nu_o} \quad (6)$$

where M_C is the molecular weight of carbon, D_{ox} is the bulk diffusion coefficient of oxygen, Sh is the Sherwood number, d_p is the particle diameter, T_m is the mean film temperature, and ν_o is the stoichiometric coefficient for oxygen.

Furthermore, γ is the change in volume during the reaction, referred to as the unit volume of oxygen, which is expressed as follows:

$$\gamma = \frac{F_{CO_2} - 1}{F_{CO_2} + 1} \quad (7)$$

where F_{CO_2} is the fraction of carbon in the particle converted to CO_2 at the particle surface. Equation 5 can be rearranged for determining the partial pressure of oxygen at the particle surface as follows:

$$P_s = \frac{P}{\gamma}\left[1 - \left(1 - \frac{\gamma P_g}{P}\right)\exp\left(\frac{\gamma q}{k_d}\right)\right] \quad (8)$$

and the char oxidation rate can be determined through a combination of eqs 3 and 8.

https://doi.org/10.1021/acsomega.1c04574
ACS Omega 2021, 6, 31132−31146

APPENDIX 2: HEAT TRANSFER OF TUBE BUNDLES IN THE CONVECTIVE PASS

For the tube bundles, the convective heat transfer coefficient, α_{conv}, is expressed as follows:

$$\alpha_{conv} = \frac{Nu_{l,bundle} k}{l} \tag{9}$$

where $Nu_{l,bundle}$ is the Nusselt number for tube bundles, k is the fluid conductivity, and l is the stream length of a single tube.

First, the Nusselt number of a single tube in cross-flow was suggested by Gnielinski[25]

$$Nu_{l,0} = 0.3 + \sqrt{Nu_{l,lam}^2 + Nu_{l,turb}^2} \tag{10}$$

where

$$Nu_{l,lam} = 0.664\sqrt{Re_{\psi,l}}\sqrt[3]{Pr} \tag{11}$$

$$Nu_{l,turb} = \frac{0.037 Re_{\psi,l}^{0.8} Pr}{1 + 2.443 Re_{\psi,l}^{-0.1}(Pr^{2/3} - 1)} \tag{12}$$

with Re being the Reynolds number for the flow, Pr being the Prandtl number of the fluid, and ψ being the void fraction.

The Nusselt number for tube bundles is expressed as

$$Nu_{l,bundle} = \frac{1 + (n-1) f_{A,in-line}}{n} Nu_{l,0} \tag{13}$$

where $f_{A,in\text{-}line}$ is the in-line tube arrangement factor and n is the number of rows. $f_{A,in\text{-}line}$ depends on the transverse pitch ratio (a), the longitudinal pitch ratio (b), and ψ, and is expressed as follows

$$f_{A,in-line} = 1 + \frac{0.7\left(\frac{b}{a} - 0.3\right)}{\psi^{1.5}\left(\frac{b}{a} + 0.7\right)^2} \tag{14}$$

The radiative heat transfer coefficient, α_{rad}, was predicted using the following equation, in which particles are not considered for simplicity[26]

$$\alpha_{rad} = \sigma \frac{\varepsilon_w}{1 - (1 - \varepsilon_w)(1 - A_V)} \frac{[\varepsilon_g T_g^4 - A_V T_w^4]}{T_g - T_w} \tag{15}$$

where σ is the Stefan–Boltzmann constant, ε is the emissivity, A_V is the gas absorptance, and T is the temperature. The subscript g denotes gas and w denotes the wall. The gas emissivity was calculated as follows

$$\varepsilon_g = \sum_{3}^{i=1} a_i(T_g)[1 - \exp(-k_{gi}(P_{H_2O} + P_{CO_2}) l_{mb})] \tag{16}$$

$$a_i(T_g) = b_{1i} + b_{2i}\left(\frac{T_g}{1000}\right) \tag{17}$$

where P_{H_2O} and P_{CO_2} are the partial pressures of H_2O and CO_2, and l_{mb} is the mean beam length. The gas absorptance was calculated using eq 16 by substituting T_g with T_w. The constants for the degree of emission of the pure gas phase (b_{1i}, b_{2i}, and k_{gi}) are shown in Table A1, which are valid at a total pressure of $P = 1$ bar and $0.5 < \frac{P_{H_2O}}{P_{CO_2}} < 2$.

Table A1. Constants for the Degree of Emission of the Pure Gas Phase[a]

i	b_{1i} (−)	b_{2i} (1/K)	k_{gi} (1/(m bar))
1	0.130	0.265	0
2	0.595	−0.150	0.824
3	0.275	−0.115	25.91

[a]This table was reproduced with permission from ref 24. Copyright 2014 Elsevier.

APPENDIX 3: NO_X FORMATION AND REDUCTION

The main reactions of the thermal NO_x (the extended Zeldovich mechanism) are as follows[27]

$$O + N_2 \rightleftharpoons N + NO \tag{18}$$

$$N + O_2 \rightleftharpoons O + NO \tag{19}$$

$$N + OH \rightleftharpoons H + NO \tag{20}$$

When the NO reburning model is applied, the NO_x reduction pathway by CH radicals is added to the existing NO reaction mechanism, and the reactions are as follows[28]

$$NO + CH_2 \xrightarrow{k_a} HCN + OH \tag{21}$$

$$NO + CH \xrightarrow{k_b} HCN + O \tag{22}$$

$$NO + C \xrightarrow{k_c} CN + O \tag{23}$$

where k_a, k_b, and k_c are the reaction rate constants for each of the above reactions given by eqs 21, 22, and 23, respectively. The concentrations of CH radicals are calculated based on the partial equilibrium during postprocessing. The reaction rates for NO_x reduction are as follows

$$R_{NO\rightarrow HCN} = (k_a \chi_1 + k_b \chi_1^2)[CH_4][NO] \tag{24}$$

$$R_{NO\rightarrow CN} = k_c \chi_1^3 \chi_2 [CH_4][NO] \tag{25}$$

When methane is used as the reburning fuel, the reaction constants are calculated in the unit of $m^3/(mol\ s)$, as follows[29]

$$k_a = 5.30 \times 10^9 T^{-1.54} \exp(-3365/T) \tag{26}$$

$$k_b = 3.31 \times 10^{13} T^{-3.33} \exp(-1815/T) \tag{27}$$

$$k_c = 3.06 \times 10^{11} T^{-2.64} \exp(-9270/T) \tag{28}$$

In eqs 24 and 25, χ_1 was assumed to be 1 and $\chi_2 = 4.43 \exp(-8060/T)$ was applied.

AUTHOR INFORMATION

Corresponding Author

Chung-Hwan Jeon − *School of Mechanical Engineering, Pusan National University, Busan 46241, Republic of Korea;* orcid.org/0000-0001-8186-3323; Phone: +82-51-510-3051; Email: chjeon@pusan.ac.kr; Fax: +82-51-512-5236

Authors

Kang-Min Kim − *School of Mechanical Engineering, Pusan National University, Busan 46241, Republic of Korea*

Gyu-Bo Kim − *School of Mechanical Engineering, Pusan National University, Busan 46241, Republic of Korea*

Byoung-Hwa Lee − *School of Mechanical Engineering, Pusan National University, Busan 46241, Republic of Korea*

https://doi.org/10.1021/acsomega.1c04574
ACS Omega 2021, 6, 31132−31146

Joon-Ho Keum − *Boryeong Power Plant, Korea Midland Power Co., Ltd., Boryeong-si, Chungcheongnam-do 33408, Republic of Korea*

Complete contact information is available at: https://pubs.acs.org/10.1021/acsomega.1c04574

Author Contributions

The manuscript was written with the contributions of all the authors. All authors approved the final version of the manuscript.

Notes

The authors declare no competing financial interest.

■ ACKNOWLEDGMENTS

This research was conducted under the framework of the Research and Development Program of the Korea Institute of Energy Research (C1-2428-01).

■ ABBREVIATIONS

CCOFA, close-coupled overfire air; CFD, computational fluid dynamics; FEGT, furnace exit gas temperature; GHG, greenhouse gas; LNG, liquefied natural gas; NO_x, nitrogen oxides; OFA, overfire air; PA, primary air; RH, reheater; SA, secondary air; SH, superheater; SOFA, separated overfire air; SO_x, sulfur oxides; SR, stoichiometric ratio; UDF, user-defined function; WB, windbox

■ REFERENCES

(1) *The 9th Basic Plan for Long-Term Electricity Supply and Demand (2020−2034)*; South Korean Ministry of Trade, Industry & Energy: Sejong, 2020.

(2) Gonzalez-Salazar, M. A.; Kirsten, T.; Prchlik, L. Review of the operational flexibility and emissions of gas- and coal-fired power plants in a future with growing renewables. *Renewable Sustainable Energy Rev.* **2018**, *82*, 1497−1513.

(3) Pescia, D. *Flexibility in Thermal Power Plants − With a Focus on Existing Coal-fired Power Plants*; Study by Agora Energiewende: Berlin, 2017.

(4) Mills, S. *Combining Solar Power with Coal-fired Power Plants, or Cofiring Natural Gas*; Report by IEA Clean Coal Centre: London, 2017.

(5) Nowling, U. Utilities Explore Dual Fuel as Low-cost Option to Full Gas Conversion. 2014, https://breakingenergy.com/2014/02/26/utilities-explore-dual-fuel-as-low-cost-option-to-full-gas-conversion (accessed Mar 18, 2021).

(6) U.S. Energy Information Administration. *Capital Cost and Performance Characteristic Estimates for Utility Scale Electric Power Generating Technologies*; U.S. Department of Energy: Washington, DC, 2020.

(7) Wendt, J. O. L.; Sternling, C. V.; Matovich, M. A. Reduction of sulfur trioxide and nitrogen oxides by secondary fuel injection. *Symp. (Int.) Combust., [Proc.]* **1973**, *14*, 897−904.

(8) Farzan, H.; Wessel, R. A. *Mathematical and Experimental Pilot-scale Study of Coal Reburning for NO Sub x Control in Cyclone Boilers*; Topical report for U.S. Department of Energy: Pittsburgh, 1991.

(9) Dusatko, G. *Gas Cofiring Assessment for Coal Fired Utility Boilers*; Technical report for Electric Power Research Institute: Chicago, 2000.

(10) Adamczyk, W. P.; Werle, S.; Ryfa, A. Application of the computational method for predicting NOx reduction within large scale coal-fired boiler. *Appl. Therm. Eng.* **2014**, *73*, 343−350.

(11) Chernetskiy, M.; Dekterev, A.; Chernetskaya, N.; Hanjalić, K. Effects of reburning mechanically-activated micronized coal on reduction of NOx: Computational study of a real-scale tangentially-fired boiler. *Fuel* **2018**, *214*, 215−229.

(12) Duke Energy. Natural gas co-firing program update. In *EPRI Combustion Workshop*, Raleigh, NC, 2017.

(13) Electric Power Research Institute. Gas co-firing studies on a tangential furnace. In *EPRI Combustion Workshop*, Raleigh, NC, 2017.

(14) Basu, P.; Kefa, C.; Jestin, L. Tangentially Fired Burners. In *Boilers and Burners: Design and Theory*; Basu, P.; Kefa, C.; Jestin, L., Eds.; Springer: New York, 2000; pp 269−301.

(15) Marx, P.; Morin, J. Conventional Firing Systems. In *Combustion Engineering Issues for Solid Fuel Systems*; Miller, B. G.; Tillman, D. A., Eds.; Academic Press: Burlington, 2008; pp 241−274.

(16) Stamey-Hall, S. *Alternative Control Techniques Document: NOx Emissions from Utility Boilers*; Technical Report for U.S. Environmental Protection Agency, 1994.

(17) Shih, T.-H.; Liou, W. W.; Shabbir, A.; Yang, Z.; Zhu, J. A new k-ϵ eddy viscosity model for high reynolds number turbulent flows. *Comput. Fluids* **1995**, *24*, 227−238.

(18) Yin, C. Effects of moisture release and radiation properties in pulverized fuel combustion: A CFD modelling study. *Fuel* **2016**, *165*, 252−259.

(19) Hurt, R. H.; Lunden, M. M.; Brehob, E. G.; Maloney, D. J. Statistical kinetics for pulverized coal combustion. *Symp. (Int.) Combust., [Proc.]* **1996**, *26*, 3169−3177.

(20) Hurt, R.; Sun, J.-K.; Lunden, M. A kinetic model of carbon burnout in pulverized coal combustion. *Combust. Flame* **1998**, *113*, 181−197.

(21) Hurt, R. H.; Mitchell, R. E. Unified high-temperature char combustion kinetics for a suite of coals of various rank. *Symp. (Int.) Combust., [Proc.]* **1992**, *24*, 1243−1250.

(22) *ANSYS Fluent Theory Guide 19.2*; ANSYS, Inc: Canonsburg, Pennsylvania, 2018.

(23) Wang, H.; Zhang, C.; Liu, X. Heat transfer calculation methods in three-dimensional CFD model for pulverized coal-fired boilers. *Appl. Therm. Eng.* **2020**, *166*, No. 114633.

(24) Schuhbauer, C.; Angerer, M.; Spliethoff, H.; Kluger, F.; Tschaffon, H. Coupled simulation of a tangentially hard coal fired 700 °C boiler. *Fuel* **2014**, *122*, 149−163.

(25) Gnielinski, V. Heat Transfer in Cross-flow around Single Rows of Tubes and through Tube Bundles. In *VDI Heat Atlas*, 2nd ed.; Stephan, P., Ed.; Springer: Berlin, Heidelberg, 2010.

(26) Vortmeyer, D.; Kabelac, S. Gas Radiation: Radiation from Gas Mixtures. In *VDI Heat Atlas*, 2nd ed.; Stephan, P., Ed.; Springer: Berlin, Heidelberg, 2010.

(27) Hill, S. C.; Douglas Smoot, L. Modeling of nitrogen oxides formation and destruction in combustion systems. *Prog. Energy Combust. Sci.* **2000**, *26*, 417−458.

(28) Kandamby, N.; Lazopoulos, G.; Lockwood, F. C.; Perera, A.; Vigevano, L. Mathematical Modeling of NOx Emission Reduction by the Use of Reburn Technology in Utility Boilers. In ASME International Joint Power Generation Conference and Exhibition, Houston, Texas, 1996.

(29) Leung, K. M.; Lindstedt, R. P. Detailed kinetic modeling of C1 — C3 alkane diffusion flames. *Combust. Flame* **1995**, *102*, 129−160.